Submitted to Geosphere theme issue on the Seismotectonics of the San Andreas fault in the San Gorgonio Pass Region

Considering fault interaction in estimates of absolute stress along faults in the San Gorgonio Pass region, southern California

Jennifer Hatch[1], Michele L. Cooke[1], Aviel Stern[1], Roby Douilly[2], David Oglesby[2]

[1]*Department of Geosciences, University of Massachusetts, Amherst, MA 01003*
[2]*Department of Earth Sciences, University of California, Riverside, CA 92521*

ABSTRACT

Present-day shear tractions along faults of the San Gorgonio Pass region can be estimated from stressing rates provided by three-dimensional forward crustal deformation models. Modeled dextral shear stressing rates on the San Andreas and San Jacinto faults differ from rates resolved from the regional loading due to fault interaction. In particular, fault patches with similar orientations and depths on the two faults show different stressing rates. We estimate the present-day, evolved fault tractions along faults of the San Gorgonio Pass region using the time since last earthquake, fault stressing rates (which account for fault interaction), and co-seismic models of the impact of recent nearby earthquakes. The evolved tractions differ significantly from the resolved regional tractions, with the largest dextral traction located within the restraining bend comprising the pass, which has not had recent earthquakes, rather than outside of the bend, which is more preferentially oriented under tectonic loading. Evolved fault tractions can provide more accurate initial conditions for dynamic rupture models within regions of complex fault geometry, such as the San Gorgonio Pass region. An analysis of the time needed to accumulate shear tractions that exceed typical earthquake stress drops shows that present-day tractions already exceed 3 MPa along portions of the Banning, Garnet Hill, and Mission Creek strands of the San Andreas fault. This result highlights areas that may be near failure if accumulated tractions equivalent to typical earthquake stress drops precipitate failure.

Keywords: San Andreas fault, San Gorgonio Pass, fault tractions, fault stressing rates, fault interaction, seismic hazard

1. INTRODUCTION

The southern San Andreas fault system consists of multiple active faults that accommodate the deformation between the North American and Pacific plates. Accurate estimates of the earthquake hazard in California require an accurate assessment of the potential for large through-going earthquakes and the ability for ruptures to propagate through fault intersections and complexities (e.g., Field et al., 2013). One region of such complexity is the San Gorgonio Pass region (SGPr), a restraining stepover along the southern San Andreas fault (Figure 1). Accurate dynamic rupture models of the SGPr that simulate potential rupture paths will help us assess the potential for large and damaging earthquakes through this region (e.g., Tarnowski, 2017; Douilly et al., 2017).

Dynamic rupture models show that, in general, the size and extent of earthquake ruptures can depend highly on the initial conditions of the model (e.g., Oglesby et al., 2005). These conditions include physical aspects, such as fault geometry and location of rupture nucleation (e.g., Lozos et al., 2012; Lozos, 2016; Tarnowski, 2017), and time-dependent aspects, such as state of stress and frictional parameters (e.g., Kame et al., 2003; Aochi and Olsen, 2004; Kase and Day, 2006; Duan and Oglesby, 2007). Dynamic rupture models typically prescribe initial shear and normal tractions by resolving the remote stress tensor, constrained from focal mechanism inversions, onto individual fault elements (e.g., Kame et al., 2003; Oglesby et al., 2003). This approach provides spatially variable ‘resolved’ tractions that capture the first-order loading of the faults but does not take into account the loading history, nor the prior stress interactions between faults. Not only can individual earthquake events change tractions along nearby faults, advancing or retarding each faults' earthquake clock (e.g., King et al., 1994; Stein, 1999; Duan and Oglesby, 2005), but interaction among neighboring active faults influences their long-term slip rates and stressing rates (Willemse and Pollard, 1998; Maerten et al., 1999; Loveless and Meade, 2011). Stressing rates on any given fault can be estimated using geodesy (e.g., Smith and Sandwell, 2006). However, the total accumulated traction along any given fault segment depends on the accumulated tractions during the interseismic period as well as nearby rupture history (e.g., Smith-Konter and Sandwell, 2009; Richards-Dinger and Dieterich, 2012; Tong et al., 2014).

To account for loading history and fault interaction and produce more accurate estimates of fault stress, we simulate deformation within the San Gorgonio Pass region using three-dimensional forward models that provide both slip rates over multiple earthquake cycles and stressing rates between earthquake events. Because we use slip rates over multiple earthquake cycles to drive models that simulate interseismic deformation, the resulting shear stressing rates incorporate the interactions between faults of the southern San Andreas fault system. The interseismic shear stressing rates along with information about time since last earthquake event can be used to estimate the shear traction on faults through the SGPr following the approach employed by Tong et al. (2014). The resulting estimates of shear traction may differ from resolving the remote stress tensor onto faults in that our models explicitly include fault interaction and fault loading from depth during the interseismic period. Furthermore, we incorporate the effects of recent earthquakes on faults near the SGPr to produce a more accurate estimate of the current stress state of this system. Using tractions that incorporate fault interaction and loading history may enhance the accuracy of dynamic rupture models, refining our insight into the nature of potential earthquake rupture propagation within the San Gorgonio Pass region.

2. REGIONAL GEOLOGY – THE SAN GORGONIO PASS REGION

Through the San Gorgonio Pass region (SGPr), deformation is partitioned onto multiple, active and nonvertical fault strands (e.g., Matti et al., 1992; Figure 1). The San Bernardino strand of the San Andreas fault lies at the northwest end of the San Gorgonio Pass. Two potential rupture pathways go through the restraining bend connecting the San Bernardino strand to the Coachella segment of the San Andreas fault. The southern pathway consists of the San Gorgonio Pass thrust, Garnet Hill strand, and Banning strand of the San Andreas fault (Figure 1). The San Gorgonio Pass thrust dips to the north and has a corrugated geometry near the Earth's surface (e.g., Matti et al., 1992). The eastern end of the San Gorgonio Pass thrust connects to the Garnet Hill and Banning strands. The north-dipping Garnet Hill and subparallel Banning strands have approximately the same strike. The northern pathway through the SGPr consists of the Mill Creek, Mission Creek, and Galena Peak strands of the San Andreas fault (Figure 1). Ongoing debate centers on the geometry and activity of these fault strands through the northern part of the SGPr (e.g., Kendrick et al., 2015; Beyer et al., 2018; Fosdick and Blisniuk, 2018). The San Jacinto fault is sub-parallel to the San Andreas fault and extends to within 2 km of the San Andreas fault at Cajon Pass. While the San Jacinto fault lies outside of the SGPr, it interacts with the San Andreas fault and consequently impacts both long-term slip rates (e.g., Herbert et al., 2014) and earthquake rupture paths (Lozos, 2016) on the San Andreas fault.

Recent paleoseismic data within the SGPr suggest that previous large through-going earthquakes have a recurrence interval of ~ 1000 years, with the most recent earthquake rupture through the San Gorgonio Pass along the southern pathway in 1400 AD (Heermance and Yule, 2017). Earthquakes along the San Bernardino strand (north of the restraining bend) and Coachella segment of the San Andreas fault (south of the bend) occur more frequently, with recurrence intervals of 200-300 years (e.g., Philibosian et al., 2011; Field et al., 2013; Onderdonk et al., 2018). The difference in recurrence intervals outside of and inside of the restraining bed suggests that previous earthquakes that have ruptured along the San Bernardino and Coachella segments terminated at the restraining bend, which may be acting as an ‘earthquake gate’. During the interseismic period since the last rupture event through the bend, shear tractions have been accumulating along faults within the SGPr. Furthermore, recent earthquakes along faults surrounding the SGPr could impact the state of stress within the San Gorgonio Pass, and thus the shear and normal tractions along the faults.

2.1 Recent earthquakes near the San Gorgonio Pass region

To calculate the stress interaction effects from past earthquakes, we consider records of three ground-rupturing earthquakes that occurred within the past 300 years near the SGPr. While many smaller earthquakes have occurred within this region, these larger ground-rupturing events have the greatest potential to impact tractions along nearby faults.

2.1.1 1992 Landers Earthquake

The Landers earthquake occurred on June 28, 1992, rupturing five fault segments, striking northwest-southeast, in the Eastern California Shear Zone (Hart et al., 1993). The interaction of these faults created a linked fault network that generated an M7.3 earthquake, which is larger than expected for any single fault involved in the rupture (Aydin and Du, 1995). The total rupture length is estimated at 85 km on the primary rupture trace (Sieh et al., 1993).

The epicenter was located on the south portion of the Johnson Valley Fault, and the rupture traveled northward along the Landers-Kickapoo, Homestead Valley, Emerson, and Camp Rock faults, crossing two extensional stepovers and one compressional stepover (e.g., Aydin and Du, 1995; Madden and Pollard, 2012), while only rupturing parts of the Johnson Valley, Emerson, and Camp Rock faults (Sieh et al., 1993). All of the involved faults were previously mapped, with the exception of the Landers-Kickapoo fault (Hart et al., 1993). The Johnson Valley and Landers-Kickapoo faults each slipped locally more than 2 m and the central portion of the Homestead Valley fault slipped more than 3 m (Sieh et al., 1993; Aydin and Du, 1995). Slip exceeded 4 m on the Emerson fault, and a maximum dextral slip of approximately 6 meters occurred on the North Emerson Fault (Bryant, 1992; Sieh et al., 1993; Bryant, 1994).

2.1.2 1812 Wrightwood Earthquake

The ~M7.5 earthquake that occurred on December 8, 1812 (here referred to as the Wrightwood earthquake), is one of the earliest earthquakes documented in the historical records of California; the rupture origin and extent are still uncertain. Evidence of this event has been observed within several paleoseismic trench sites along the San Andreas fault north of Cajon Pass (Weldon and Sieh, 1985; Seitz et al., 1997; Biasi et al., 2002; Fumal et al., 2002; Weldon et al., 2002), with a maximum dextral slip of 4-6 m and possible northern rupture extent ~100 km north of the Cajon Pass (Bemis et al., 2016). The southern extent of rupture is not well constrained. The most recent event recorded at Plunge Creek on the San Bernardino strand (site 3 Fig.1) is dated to within the 1600s (McGill et al., 2002), but minor slip on secondary structures farther south along the San Bernardino strand, near Burro Flats (site 4 Fig. 1), dates to the early 1800s (Yule and Howland, 2001). Several paleoseismic sites along the northernmost strand of the San Jacinto fault record 1.8-3 m of slip during an early 1800s earthquake event (Kendrick and Fumal, 2005; Onderdonk et al., 2013; Onderdonk et al., 2015). Several have suggested the plausibility of the 1812 earthquake jumping the < 2 km extensional stepover between the San Andreas and San Jacinto faults (Figure 1) and involving both faults (Onderdonk et al., 2013; Onderdonk et al., 2015; Rockwell et al., 2015). Lozos (2016) used dynamic rupture models to investigate rupture scenarios that best fit the paleoseismic evidence and historical accounts of the Wrightwood earthquake. The models of Lozos (2016) suggest that the Wrightwood earthquake nucleated near Mystic Lake on the San Jacinto fault (site 8 Fig. 1), produced a maximum of 6 m of slip near Colton, and propagated north onto the San Andreas fault (maximum of 4-5 m of slip between Cajon Pass and Wrightwood).

2.1.3 1726 Coachella Valley Earthquake

The Coachella segment of the southern San Andreas fault has not experienced a large earthquake in historical time. Paleoseismic studies reveal that the most recent earthquake is dated to 1726 ± 7 (Rockwell et al., 2018), with a possible rupture trace extending from Salt Creek site along the Salton Sea (site 7 Fig. 1; Sieh and Williams, 1990) to the Thousand Palms oasis site on the Mission Creek strand (site 5 Fig. 1; Fumal et al., 2002), with at least 2 m of dextral offset at the Indio site on the Coachella segment (site 6 Fig. 1; Sieh, 1986).

3. METHODS

We use Poly3D, a quasi-static, three-dimensional boundary element method code, to simulate loading and interseismic deformation along the southern San Andreas fault system. Poly3D solves the relevant equations of continuum mechanics to calculate stresses and displacements throughout the model (e.g., Thomas, 1993; Crider and Pollard, 1998). Faults are discretized into triangular elements of constant slip (no opening/closing is permitted) within a linear-elastic half-space. The element size along the faults of the San Gorgonio Pass region (SGPr) average ~4 km and allow for our models to capture fault irregularities as small as ~10 km. We simulate the active fault geometry of the southern San Andreas fault, the San Jacinto fault, and the Eastern California Shear Zone (Figure 2) based on the Southern California Earthquake Center’s Community Fault Model (CFM) version 4.0 (Plesch et al., 2007; Nicholson et al., 2017). The CFM is compiled from geologic mapping, seismicity, and geophysical data. While the CFM has been updated to version 5.2, the interpreted active fault geometry of the San Gorgonio Pass region is still under debate (e.g., Kendrick et al., 2015; Beyer et al., 2018; Fosdick and Blisniuk, 2018). We use version 4.0 of the CFM but include fault geometry modifications that serve both to improve the representation of the mapped active fault geometry and to improve the match of model and geologic uplift patterns and slip rates in the San Gorgonio Pass region (e.g., Cooke and Dair, 2011; Herbert and Cooke, 2012; Fattaruso et al., 2014; Beyer et al., 2018).

Faults in the CFM are defined to the base of the seismogenic crust. To simulate long-term and interseismic deformation, we extend the faults down to a freely slipping, horizontal basal crack at 35 km depth that simulates distributed deformation below the seismogenic zone (Marshall et al., 2009). This modification eliminates artifacts that develop when the long-term slip rates go to zero at the base of the CFM-defined faults (Figure 2). Across many earthquake cycles, deformation patterns are primarily controlled by fault geometry (e.g., Dawers and Anders, 1995; Fay and Humphreys, 2005; Herbert and Cooke, 2012). Therefore, to capture the first-order loading of active faults, we do not consider potential secondary impacts of heterogeneous and/or anisotropic rock properties.

We prescribe the tectonic loading on the boundaries of the model base, far from investigated faults. Following Beyer et al. (2018), we implement an iterative technique that ensures a uniform tectonic velocity, determined from geodetic estimates (DeMets and Dixon, 1999) at the model edges that are sub-parallel to the plate boundary (sides labeled I on Figure 2) and a linear velocity gradient at the models edges that cross the plate boundary (sides labeled II on Figure 2). The iterative approach of Beyer et al. (2018) ensures that applied velocities are within ~1% of the desired tectonic loading. For faults that extend beyond our model area (San Andreas, San Jacinto, and Cucamonga-Sierra Madre fault systems), we apply slip rates to distal edge patches of these faults to prevent non-zero slip rates on these faults at the edge of our model. We apply 35 mm/yr dextral slip to the San Andreas fault at the northwestern edge of the model (Weldon and Sieh, 1985). At the southeastern edge, we prescribe 25 mm/yr dextral slip to the San Andreas fault and 10 mm/yr dextral slip to the San Jacinto fault (e.g., Sharp, 1981; Becker et al., 2005; Fay and Humphreys, 2005; Meade and Hager, 2005). Because of complex fault geometry and interaction among faults, deformation within the SGPr is not impacted significantly by variations in the partitioning of slip rates between the San Andreas and San Jacinto faults at this model edge (Fattaruso et al., 2014). We apply 1.6 mm/yr reverse slip (McPhillips and Scharer, 2018) to the western edge of the modeled Cucamonga fault to account for deformation along the Sierra Madre fault not included in our model.

We use a two-step modeling approach to estimate the interseismic stressing rates along the southern San Andreas fault system. The first model simulates deformation over many earthquake cycles (steady state model) providing slip-rate information to a second model (interseismic model) that simulates the build-up of stress between earthquakes due to constant slip below the locking depth. In the steady state model, tectonic loading is prescribed along the model edges at the base of the model, far from the investigated faults. The faults throughout the model have zero shear traction and slip freely in response to tectonic loading and fault interaction. This zero-shear traction simulates the low dynamic strength of faults during rupture (e.g., Di Toro et al., 2006; Goldsby and Tullis, 2011). We simulate interseismic deformation by applying the distribution of slip rates determined with the steady state model to fault surfaces below the prescribed locking depth and lock fault elements above the locking depth. The abrupt transition from locked to slipping at the specified locking depth used here produces stresses that are unreliable within one element of the transition, or ~ 5 km. We use a locking depth of 25 km to ensure that our model results provide reliable fault tractions to about 20 km depth that can be used within dynamic rupture simulations within the full depth of the seismogenic crust.

3.1 Estimating the impact from nearby recent earthquakes

We simulate the 1992 Landers earthquake, 1812 Wrightwood earthquake, and 1726 Coachella Valley earthquakes by prescribing the interpreted co-seismic slip distribution associated with each earthquake (e.g., Sieh, 1986; Hart et al., 1993; Onderdonk et al., 2015) to the modeled fault surfaces. We segment the rupture surface into multiple vertical segments and prescribe each segment a uniform slip according to the observations at the rupture trace (Figure 4). All other faults in the model are locked, and we do not consider the effect of tectonic loading while simulating each earthquake due to the short rupture time. The resulting static stress changes due to each earthquake alters tractions along the faults within the SGPr.

3.2 Estimating evolved tractions

The interseismic model determines stressing rates due to deep movement below the seismogenic crust and uses these stressing rates to calculate current shear tractions along the fault segments of the southern San Andreas fault within the SGPr using the time since the last rupture. Estimating both shear and normal tractions from stressing rates requires an assumption on how such accumulated tractions may dissipate with time. This approach relies on the premise that shear tractions that accumulate during the interseismic period are released during earthquake events. Because normal tractions that accumulate in the interseismic period, such as within restraining bends, are not necessarily relieved upon fault slip, models of earthquake cycles require dissipation mechanisms in order to avoid singular-valued normal tractions. Duan and Oglesby (2006) simulate multiple earthquake cycles by coupling a viscoelastic interseismic model with an elastic dynamic rupture model, such that normal stresses are relaxed during the interseismic period in the viscoelastic model and used as input to the dynamic rupture model. Alternatively, the Rate and State Earthquake Simulator (RSQSIM) employs a constant, but spatially variable normal stress distribution and disregards accumulated normal tractions (e.g., Richards-Dinger and Dieterich, 2012). Here, we follow the approach of RSQSIM and do not carry the normal stressing rates through the rest of the analysis.

To estimate the shear traction that evolves over the earthquake cycle, henceforth called the evolved shear traction, we follow Tong et al. (2014) and use the stressing rate information from the interseismic model and the time since last event for each fault. In this approach, we only consider large ground-rupturing events that are preserved in the paleoseismic record. The approach analyzes a coseismic stress drop corresponding to the change from static friction to dynamic friction during large ground-rupturing earthquakes (shaded region in Figure 3). If the dynamic strength of the fault is near zero, a complete stress drop is associated with these events. Such complete stress drop is consistent with recent field measurements of low temperatures along recently ruptured fault surfaces, a result of a very low dynamic friction (e.g., Carpenter et al., 2012, Fulton et al., 2013, Li et al., 2015), as well as high-speed laboratory frictional experiments cited above. Consequently, the associated shear traction at any time in the earthquake cycle is

$$\tau = \dot{\tau} \cdot t \qquad (1)$$

where τ is the evolved shear traction, $\dot{\tau}$ is the shear stressing rate and t is the time since last event. We sum the evolved shear tractions calculated by Equation 1 and the static stress changes due to nearby earthquakes to produce the present-day evolved shear tractions along the faults within the SGPr. This simplified approach to estimate the distribution of present-day shear tractions may provide more accurate initial conditions than the approach employed by dynamic rupture models of estimating tractions by resolving the remote loading onto the faults because the evolved tractions also incorporates both loading history and fault interaction, by including long term slip rates at depth and recent nearby earthquake events (Figure 3).

3.3 Consideration of geometric and tectonic uncertainty

Using models of deformation over multiple earthquake cycles, Beyer et al. (2018) compared the slip rate distribution from six plausible active fault configuration models to available geologic slip rate data. The analysis revealed that two active fault configurations provide the best fit to the geologic observations. For this study, we use both of the two best-fit models: the *Inactive Mill Creek* and *West Mill Creek* models from Beyer et al. (2018). The most pronounced fault geometry difference between the two configurations is the addition of a through-going Mission/Mill Creek strand through the northern part of the SGPr in the *West Mill Creek* model. Here, we present the results of the *Inactive Mill Creek* model geometry, and the

Supplemental Material contains the results of the *West Mill Creek* model geometry. Following Herbert and Cooke (2012), Beyer et al. (2018) also tested each of the plausible fault configurations under a range of reasonable tectonic loading (45-50 mm/yr at 340˚-345˚; DeMets and Dixon, 1999); for this study, we use the mean slip rate from the end members of permissible tectonic loadings.

4. RESULTS

We present the interseismic stressing rates for faults of the San Gorgonio Pass region (SGPr) and show the impact of fault interaction on these rates. We analyze the results of the models that simulate three recent ground-rupturing earthquakes and the impact of these earthquakes on fault tractions within the SGPr. We then calculate the total evolved shear tractions that incorporate the impacts of both fault interaction and loading history.

4.1 Stressing rates

Maps of interseismic shear stressing rate along the southern San Andreas fault reveal how the fault geometry controls the stressing rate distribution (Figure 5). Figure 5 shows stressing rates for the *Inactive Mill Creek* model configuration (Figure 5A and 5C) and the difference in stressing rates between the two plausible active fault geometries (Figure 5B and 5D). Dextral shear stressing rates are larger (maximum 12 kPa/yr) than the reverse-shear stressing rates (maximum ~3 kP/yr) along the San Andreas fault. Furthermore, portions of the faults parallel to the overall plate motion, outside of the restraining bend, have greater dextral stressing rate than faults within the bend. Dextral shear stressing rates are largest along the San Bernardino and Mission Creek strands of the SAF and decrease within the restraining bend of the SGPr (Figure

5A). The San Gorgonio Pass thrust has an undulating strike and small sinistral shear stressing rates occur locally along patches of the western San Gorgonio Pass thrust where the strike is less than ~265˚. The reverse-shear stressing rates are near zero outside the restraining bend and increase within the bend along north-dipping fault strands that strike obliquely to the plate motion and accommodate uplift (Figure 5C). Stressing rates increase with depth, consistent with the deep slip that is applied to faults in the interseismic model. The difference in stressing rates between the two best-fitting model geometries (Figure 5B and 5D) are lower than 1 kPa/yr and indicate that the *West Mill Creek* fault geometry produces higher dextral stressing rates (blue) throughout most of the region. The greatest difference in reverse-shear stressing rates is limited to within and just outside the bend. We only consider the *Inactive Mill Creek* fault geometry for the rest of our analysis, and consequently, reported shear tractions may underestimate by ~2% shear tractions if the true active fault geometry is closer to the configuration of our *West Mill Creek* model.

To the first order, the strike-parallel shear stressing rate along the southern San Andreas fault correlates with the orientation of the fault segments relative to the applied model loading that simulates plate motions. Previous models of the region have shown significant interaction between the San Andreas and San Jacinto faults (Herbert et al., 2014; Fattaruso et al, 2014), so we expand the analysis of stressing rates to include both of these faults in order to investigate the influence of fault interaction on stressing rates. The model produces different interseismic dextral shear stressing rates along similarly oriented portions of the San Andreas and San Jacinto faults. Figure 6 shows a gridded surface fit through model data points (white circles) of dextral stressing rates for different strikes and depths of the San Andreas (Figure 6A) and San Jacinto faults (Figure 6B). Stressing rates for both faults increase with depth, and in general, dextral stressing rates are higher on the San Andreas fault than on the San Jacinto fault for locations with the same strike and depth. For the San Andreas fault, maximum dextral stressing rate occurs at strikes between 300°-305°. Relative to the San Andreas, the variation of dextral stressing rate with strike along the San Jacinto fault is more subdued, but the distribution shows a maximum strike stressing rate along segments that strike ~310°. Both of these maximum shear orientations differ from the orientation expected from resolving the regional stress tensor (black line in Figure 6). The difference between dextral stressing rates along the San Andreas and San Jacinto faults and the expected distribution from resolved tractions demonstrates the strong impact of fault interaction on the distribution of fault stressing rates.

The impact of fault interaction is also demonstrated in the relative stressing rates on the Banning and Mission Creek strands, which differs between the two plausible fault configurations (Figure 5). The presence of a through-going Mission Creek fault in the *West Mill Creek* model geometry (Figure S1) shifts strike-parallel shear stressing rates from the Banning strand to the Mission Creek strand by ~ 0.1 kPa/yr. These differences in stress accumulation rates over the interseismic period demonstrates that fault interaction impacts the distribution of accumulated tractions along faults within a complex system.

4.2 Impact of stresses from regional earthquakes

To assess the impact of the recent nearby earthquakes along faults within the SGPr, we numerically simulate three ground-rupturing earthquakes. We simulate the Landers Earthquake, Wrightwood Earthquake, and Coachella Valley Earthquake and examine the static stress change due to each event (Figure 7). Because we do not consider the potential relaxation of these crustal stresses over time (e.g., Pollitz and Sacks, 2002), the fault tractions from earthquakes modeled provide an upper bound to expected tractions.

The modeled static stress change from the 1992 Landers earthquake impacts tractions along faults within the San Gorgonio Pass restraining bend. The change in dextral tractions (positive) reach a maximum of ~0.1 MPa, along the San Gorgonio Pass thrust and a change in sinistral tractions (negative) of up to 0.15 MPa on the southern Garnet Hill, Banning, and Mission Creek strands of the SAF (Figure 7A). The San Gorgonio Pass region lies in the extensional quadrant of the Landers rupture, and as a result, the fault strands within the bend are loaded with normal dip-slip tractions of ~ 0.13 MPa. This dip-slip traction change effectively reduces the accumulated long-term reverse dip-slip traction on these faults.

Change in co-seismic dextral tractions due to the 1812 Wrightwood earthquake increase the most (1.3 MPa) just south of the rupture limit on the San Bernardino strand, while the southernmost portion of the San Bernardino strand experiences sinistral traction changes of ~ 0.25 MPa (Figure 7B). The western San Gorgonio Pass thrust is loaded with dextral tractions (~ 0.4 MPa), while the Garnet Hill, Banning and Mission Creek strands experience slight (<0.1 MPa) increases in sinistral shear tractions. Furthermore, the western-most extent of the San Gorgonio Pass thrust has normal dip-slip shear, while the rest of the thrust and Garnet Hill strand has reverse dip-slip shear. These complex fault stressing patterns result from the location and orientation of the faults in relation to the Wrightwood rupture path. The close proximity of the dextral slip on the SJF to the subparallel fault strands of the SAF results in sinistral co-seismic traction changes on the SAF, which sits in the stress shadow of the Wrightwood earthquake.

Traction changes imposed on the San Gorgonio Pass fault strands due to the 1726 Coachella Valley earthquake reach ~ 1 MPa on the Mission Creek ahead of the rupture termination and ~ 0.8 on the Banning strands near the junction with the Coachella segment

(Figure 7C). Dextral tractions of up to ~ 0.1 MPa extend into the restraining bend. While these nearby earthquakes are shown here to impact the SGPr, all the resulting static stress changes due to these earthquakes are small compared to the total tractions accumulated along these faults during the interseismic period.

4.3 Estimate evolved stresses

Paleoseismic data provide estimates for the time since last event, *t*, along active faults (e.g., Biasi et al., 2009; Table 1). We estimate the total present-day traction along each fault segment by summing the tractions from Equation 1 with the static traction change of each nearby earthquake. For the San Bernardino segment, we use time since last event from the compiled earthquake data of Biasi et al. (2009). Paleoseismic sites at Pitman Canyon (site 2 Fig. 1), Plunge Creek (site 3 Fig. 1), and Wrightwood (site 1 Fig. 1) provide a mean *t* of 207 years for the San Bernardino segment. Paleosismic constraints from the Thousand Palms Oasis site (site 5 Fig. 1; Fumal et al., 2002) is used for the Mission Creek strand and the Coachella site (site 6 Fig. 1; Philibosian et al., 2011) for the Coachella segment. These studies are in agreement that the last rupture event occurred circa 1680. This event has been re-dated by Rockwell et al. (2018) to be around the year 1726 ± 7. For the San Gorgonio Pass thrust, Banning, and Garnet Hill strands of the SAF, we use an earthquake rupture year of 1400 (Heermance et al., 2017; Yule et al., 2014).

Fault strand(s)	Paleoseismic Site(s)	Most recent EQ Year (AD)	Time since last event (yr)
San Bernardino	Pitman Canyon/Plunge Creek/Wrightwood *(Biasi et al.,2009)*	1812	207
Banning/SGPT/ Garnet Hill	Millard Canyon (*Heermance et al.,* 2017, *Yule et al.*, 2014)	1400	619
Mission Creek/Coachella	1000 Palms/Coachella *(Fumal et al., 2002; Philibosian et al., 2011;*	1726	293

	Rockwell et al., 2018)		

Table 1: Time since last event data used to calculate absolute shear stress from the interseismic stressing rate.

Due to the variable time since last earthquake event across faults of the SGPr, the evolved shear traction distribution along the fault surfaces (Figure 8A) differs significantly from the shear stressing rate distributions (Figure 5). Whereas dextral-shear stressing rates are lower along the north-dipping fault surfaces within the SGPr restraining bend than on fault surfaces outside of the bend (Figure 5A), the longer t for the faults within the restraining bend increases the total accumulated dextral shear traction within the bend relative to other faults (Figure 8A). Similarly, although the Coachella segment and the San Bernardino strand of the SAF have greater dextral stressing rates than the restraining segment, the more recent rupture of these segments in the 1726 and 1812 events, respectively, reduces the accumulated tractions outside the bend. The largest evolved dextral shear tractions arise along the Banning and Garnet Hill strands of the SAF near the juncture with the Coachella segment of the SAF (Figure 8A). Regions of high dextral shear traction also arise along portions of the San Gorgonio Pass thrust. The evolved reverse shear tractions are greatest along the San Gorgonio Pass thrust within the restraining bend. We note that if the true active fault geometry is closer approximated by the alternative fault configuration (Figure S1), the total evolved shear tractions may be underestimated by up to 2%.

These evolved shear tractions take into account fault interaction (Figure 6), the t for each fault strand (Table 1), and the impact of recent nearby earthquakes (Figure 7). To assess the impact of fault history and interaction, we compare the evolved dextral shear traction (Figure 8A) to the fault tractions that result from resolving the regional stress tensor constrained from focal mechanism inversions onto the faults (Figure 8B). Following Tarnowski (2017), we use the orientation of the stress field and relative magnitude of the principal stress axes from Hardebeck and Hauksson (2001) and the stress ratio, Aϕ (Simpson, 1997), of 1.5, which indicates a mixed strike-slip and thrust stress regime. The resulting stress tensor is scaled such that the change from static to dynamic friction results in a 3 MPa stress drop (e.g., Tarnowski, 2017) in order to represent the fault loading conditions preceding a large earthquake rupture. The larger magnitude of the resolved dextral shear tractions compared to the evolved tractions is due to the scaling of the regional stress to produce failure and a 3 MPa stress drop with a dynamic friction of 0.1. The evolved tractions to the current year (2019) are not explicitly at failure and these tractions exclude those required for dynamic sliding (non-shaded region of Figure 3). Consequently, we focus our comparison on the patterns of the evolved and resolved stresses rather than the absolute level of stress. The resolved tractions have greater lateral heterogeneity as the tractions range from 10 MPa dextral to -5 MPa sinistral shear traction, where portions of the San Gorgonio Pass thrust receives sinistral shear from resolved loading. In contrast, the evolved tractions show dextral shear tractions everywhere on faults of the SGPr. Whereas the evolved shear tractions increase with depth, the remote stress tensor is not resolved for different depths.

5. DISCUSSION

Here we discuss the impact of including fault interaction and the effects of recent nearby earthquakes on fault tractions, and the implications of this study's findings for seismic hazard assessment.

5.1 Resolved tractions likely oversimplify initial conditions for rupture

Rupture propagation within dynamic models highly depends on the initial conditions used for the model (e.g., Kame et al., 2003; Duan and Oglesby, 2007; Lozos et al., 2012). These models have the power to simulate potential rupture size and extent, as well as potential rupture paths (e.g., Oglesby et al., 2003). Most rupture dynamic studies either use a homogeneous regional stress field (e.g., Lozos et al., 2012) or a regional stress field with spatially rotating principal stress (e.g., Aochi and Fukuyama, 2002) to estimate the initial shear tractions on fault segments. Resolving the regional stress tensor onto faults does not account for fault interaction or the rupture history of each fault. Whereas these effects may be minimal in regions with planar faults, we show here that within regions of fault complexity, fault interaction and loading history can advance, or retard, the fault towards failure. Prescribing tractions that incorporate the effects of fault interaction and the loading history of each fault may improve the accuracy of dynamic rupture models.

Due to fault interactions over multiple earthquake cycles and the variable time since last earthquake event across faults of the SGPr, the evolved shear traction distribution along the fault surfaces (Figure 8A) differs from the tractions resolved from the regional stress state (Figure 8B). Whereas resolved dextral-shear tractions are lower along the north-dipping fault surfaces within the SGPr restraining bend than on faults outside of the bend (also seen in the stressing rates in Figure 5), the longer *t* for the faults within the restraining bend increases the total dextral shear traction compared to other faults (Figure 8A). Similarly, the more recent ruptures of the 1726 and 1812 earthquake events reduce the accumulated tractions outside the bend, but not within. The largest dextral shear tractions arise along the Banning and Garnet Hill strands of the SAF, especially near the juncture of the Banning strand with the Coachella segment of the SAF (Figure 8A). Furthermore, the evolved stresses do not produce enigmatic left-lateral loading on portions of the San Gorgonio Pass thrust of the resolved stresses. These structures do not show surface evidence for left-lateral slip (Yule and Sieh, 2003). Consequently, the pattern of consistent dextral shear traction produced by the evolved stresses that include fault interaction and interseismic loading agrees with geologic evidence. Including evolved stress state for initial conditions within dynamic rupture models can produce more accurate assessment of rupture behavior along complex fault systems.

5.2 Implications for seismic hazard

To assess how close the faults of the San Gorgonio Pass region (SGPr) are to failure within our model of evolved fault tractions, we analyze the time until failure for each fault element. To consider this, we calculate how many years are required from the present day to accumulate evolved net shear tractions equivalent to typical earthquake stress drops of 3 MPa (Figure 9A) and 10 MPa (Figure 9B) (e.g., Allman and Shearer, 2009; Goebel et al., 2015). Using this criterion, fault elements on the easternmost Banning, Garnet Hill, and Mission Creek strands currently exceed 3 MPa at the base of the model (ellipse in Figure 9A). When using 10 MPa for the accumulated traction required to trigger the next earthquake, the first fault element to fail is on the San Bernardino strand at 584 years from now (ellipse in Figure 9B). The difference in vulnerable position within the fault system owes to the greater stressing rate along the San Bernardino strand compared to the other faults.

The time since last ground rupturing earthquake event for fault strands within and just outside the restraining bend are near or greater than the estimated recurrence interval for these fault strands, and paleoseismic studies in this region suggest these faults are probably overdue, or close to failure (Philibosian et al., 2011; Rockwell et al., 2018; Onderdonk et al., 2018). Consequently, while 3 MPa represents a low stress drop in the SGPr (Goebel et al., 2015), this lower stress drop implies that these faults are close to failure, which is consistent with earthquake clock and recurrence intervals of these faults.

6. CONCLUSIONS

We use three-dimensional crustal deformation models to estimate present-day fault tractions in the San Gorgonio Pass region. The models that estimate interseismic stressing rates are loaded with deep slip rates determined from a multiple-earthquake-cycle model that explicitly includes fault interaction. Consequently, the interseismic stresses incorporate both regional tectonic loading and fault interaction. A gradient of increasing shear stressing rates with depth emerges from our models that is consistent with deep interseismic deformation. To investigate the role of fault interaction within our models, we compare our modeled dextral shear stressing rates for the San Andreas and San Jacinto faults, which have similar orientation. Subsequently, the interseismic stressing rates would be similar on the two faults if based solely on orientation with respect to remote loading. Significant differences in the patterns of stressing rates along patches of the San Andreas and San Jacinto faults with similar orientation and depth arise due to the interaction between these two faults.

The total evolved present-day shear tractions along the fault include both the accumulated stressing rates since the last earthquake event and the impact of nearby earthquakes. We simulate recent nearby ground-rupturing earthquakes with co-seismic models to investigate the impact of these rupture events on the stress state along the San Andreas fault within the San Gorgonio Pass region. The pattern of total evolved fault tractions differs from that of the interseismic stressing rates. Tractions are higher within the restraining bend than outside the bend because of the longer time since last event on these faults. Fault strands within the restraining bend have been loading for twice as long as the Coachella segment to the south and three times as long as the San Bernardino strand to the north. Comparison of our evolved tractions to the tractions resolved from the local stress field shows distinct differences. While the linear gradient with depth emerges from our models, the resolved tractions are not depth dependent, and the gradient must be added. Because the evolved tractions account for loading history, the largest tractions occur within the restraining bend, which has the longer time since last event.

We investigate the time needed for the accumulated net shear traction on each fault element to exceed 3 MPa and 10 MPa, typical coseismic stress drop values. Because the interseismic stress rates differ for faults throughout the San Gorgonio Pass region, the location and timing of potential failure depends on the stress drop value used as the shear traction threshold. Assuming a lower stress drop value shows that faults in the San Gorgonio Pass are currently at failure, whereas higher stress drop values do not.

This approach provides a more heterogeneous, more accurate representation of the current stress state along the southern San Andreas fault than a simple regional stress tensor. In regions of complex fault geometry such as the San Gorgonio Pass region, an 'earthquake gate', the potential for a through-going rupture is unclear and stress state may have a large control on rupture behavior. Our evolved fault tractions can provide more realistic initial conditions for dynamic rupture models of these regions, and therefore improve seismic hazard assessments.

ACKNOWLEDGEMENTS

The project was funded by USGS External Research Program grant G15AP00068, NSF grant EAR 1623637, and the Southern California Earthquake Center (Contribution No. 9076). SCEC is funded by NSF cooperative agreement EAR-1600087 and USGS cooperative agreement G17AC00047.

FIGURE CAPTIONS

Figure 1. Map of the San Gorgonio Pass region (SGPr). While there has not been a rupture event in the SGPr since ~1400 AD, recent nearby earthquakes may impact the stress within the bend. Fault traces of the San Andreas fault are labeled (GP – Galena Peak, SGPT – San Gorgonio Pass Thrust). Rupture traces considered in this study are highlighted: Landers earthquake (dark red), Wrightwood earthquake (red), Coachella Valley earthquake (orange), and 1400 event (yellow). Paleoseismic sites are numbered as such: 1 – Wrightwood, 2 – Pitman Canyon, 3 – Plunge Creek, 4 – Burro Flat, 5 – Thousand Palms, 6 – Indio, 7 – Salt Creek, 8 – Colton, and 9 – Mystic Lake.

Figure 2. Northward oblique view of the model setup. Tectonic loading is prescribed at the boundaries of the model base, such that sides labeled (I) have a uniform tectonic velocity parallel to the plate boundary and sides labeled (II) are prescribed a linear gradient in the tectonic loading across the plate boundary. The shear traction-free faults slip freely in response to the loading and fault interaction. Black box outlines the San Gorgonio Pass region. SAF - San Andreas fault; SJF - San Jacinto fault.

Figure 3. Schematic sketch of fault loading through time. During the interseismic period, the earthquake clock of a fault can be advanced or retarded by earthquakes on other nearby faults. If the dynamic strength of the fault is near zero, then the stress drop associated with the change from static to dynamic friction is a complete stress drop.

Figure 4. Northward oblique view of the San Gorgonio Pass region showing the distribution of the applied slip (in meters) associated with the nearby 1992 Landers (dark red), 1812 Wrightwood (red), and 1726 Coachella Valley (orange) earthquakes.

Figure 5. Modeled interseismic stressing rates along faults within the San Gorgonio Pass. This region is primarily loaded in dextral shear (red in A). North-dipping faults are also loaded in reverse dip slip (red in C). B and D show the difference in stressing rates between the two plausible fault configurations of Beyer et al. (2018); difference is slip rate from *Inactive Mill Creek* minus slip rate from *West Mill Creek* model configuration.

Figure 6. Modeled dextral stressing rates plotted with depth and fault strike for the A) San Andreas fault and B) San Jacinto fault. Model results are plotted as white circles, and a best-fit surface is fitted through the data (background grid). Patches along the two faults with similar orientation and depth have different values of shear stressing rates due to fault interaction. The orientations of magnitude of dextral shear stressing rate for both faults differ from the maximum shear direction predicted from the regional stress tensor (vertical black lines).

Figure 7. Static stress changes from modeled recent, nearby earthquakes resolved as right-lateral tractions along faults of the SGPr. The Landers earthquake (A) increased dextral shear tractions along the San Bernardino strand and San Gorgonio Pass thrust, and decreased dextral shear tractions along the Garnet Hill, Banning, and Mission Creek strands. The Wrightwood earthquake (B) produces a complex change in tractions. The earthquake increased dextral shear tractions just east of the rupture termination on the San Bernardino strand but decreased dextral shear tractions further east due to the interaction with the neighboring San Jacinto fault, which had dextral slip. The Coachella Valley earthquake (C) increased dextral shear tractions on the

easternmost Mission Creek and Banning strands.

Figure 8. Evolved (A) and Resolved (B) right-lateral tractions along faults of the SGPr. The increasing shear traction with depth emerges from the evolved stresses due to deep slip in the interseismic models. The resolved tractions show greater lateral variation than the evolved tractions. Arrows indicate the direction of principle compression.

Figure 9. Faults of the SGPr colored by years until failure. (A) shows time until net shear tractions since the last earthquake exceed 3 MPa. With this criterion, fault elements on the Banning, Garnet Hill, and Mission Creek strands are currently at failure. (B) shows time until net shear tractions since the last earthquake exceed 10 MPa. Under this assumption, the first fault element to fail is on the San Bernardino strand at 584 years from present. Ellipses highlight the first elements to fail.

REFERENCES

Allmann, B.P. and Shearer, P.M., 2009. Global variations of stress drop for moderate to large earthquakes. *Journal of Geophysical Research: Solid Earth*, *114*(B1).

Aochi, H. and Fukuyama, E., 2002. Three-dimensional nonplanar simulation of the 1992 Landers earthquake. *Journal of Geophysical Research: Solid Earth*, *107*(B2), pp.ESE-4.

Aochi, H. and Olsen, K., 2004. On the effects of non-planar geometry for blind thrust faults on strong ground motion. In *Computational Earthquake Science Part II* (pp. 2139-2153). Birkhäuser, Basel.

Aydin, A. and Du, Y., 1995. Surface rupture at a fault bend: The 28 June 1992 Landers, California, earthquake. *Bulletin of the Seismological Society of America*, *85*(1), pp.111-128.

Becker, T.W., Hardebeck, J.L. and Anderson, G., 2005. Constraints on fault slip rates of the southern California plate boundary from GPS velocity and stress inversions. *Geophysical Journal International*, *160*(2), pp.634-650.

Bemis, S., Scharer, K.M., Dolan, J.F. and Rhodes, E., 2016. The Elizabeth Lake paleoseismic site: Rupture pattern constraints for the past~ 800 years for the Mojave section of the south-central San Andreas Fault. In *7th international INQUA workshop on paleoseismology, active tectonics and archaeoseismology*.

Beyer, J., Cooke, M.L. and Marshall, S.T., 2018. Sensitivity of deformation to activity alongthe Mill Creek and Mission Creek strands of the southern San Andreas fault. *Geosphere*, 14(6), pp.2296-2310.

Biasi, G.P., Weldon, R.J., Fumal, T.E. and Seitz, G.G., 2002. Paleoseismic event dating and the conditional probability of large earthquakes on the southern San Andreas fault, California. *Bulletin of the Seismological Society of America*, *92*(7), pp.2761-2781.

Biasi, G.P. and Weldon, R.J., 2009. San Andreas fault rupture scenarios from multiple paleoseismic records: Stringing pearls. *Bulletin of the Seismological Society of America*, 99,2A, pp. 471-498.

Bryant, W.A., 1992. Surface rupture along the Johnson Valley, Homestead Valley, and related faults associated with the M 7.5 28 June 1992 Landers Earthquake. *Div. Mines Geol. Fault Eval. Rep*, *234*.

Bryant, W.A., 1994. Surface fault rupture along the Homestead Valley, Emerson, and related faults associated with the Mw 7.3 28 June 1992 Landers earthquake. *Fault Eval. Rep.*

FER, *239*, p.18.
Carpenter, B.M., Saffer, D.M. and Marone, C., 2012. Frictional properties and sliding stability of the San Andreas fault from deep drill core. *Geology*, *40*(8), pp.759-762.
Cooke, M.L. and Dair, L.C., 2011. Simulating the recent evolution of the southern big bend of the San Andreas fault, southern California. *Journal of Geophysical Research: Solid Earth*, *116*(B4).
Crider, J.G. and Pollard, D.D., 1998. Fault linkage: Three-dimensional mechanical interaction between echelon normal faults. *Journal of Geophysical Research: Solid Earth*, *103*(B10), pp.24373-24391.
Dawers, N.H. and Anders, M.H., 1995. Displacement-length scaling and fault linkage. *Journal of Structural Geology*, *17*(5), pp.607-614.
DeMets, C. and Dixon, T.H., 1999. New kinematic models for Pacific-North America motion from 3 Ma to present, I: Evidence for steady motion and biases in the NUVEL-1A model. *Geophysical Research Letters*, *26*(13), pp.1921-1924.
Di Toro, G., Hirose, T., Nielsen, S. and Shimamoto, T., 2006. Relating high-velocity rock-friction experiments to coseismic slip in the presence of melts. *Geophysical Monograph-American Geophysical Union*, *170*, p.121.
Douilly, R., Oglesby, D.D., Cooke, M.L. and Beyer, J.L., 2017, December. Dynamic Models of Earthquake Rupture along branch faults of the Eastern San Gorgonio Pass Region in CA using Complex Fault Structure. In *AGU Fall Meeting Abstracts*.
Duan, B. and Oglesby, D.D., 2005. Multicycle dynamics of nonplanar strike-slip faults. *Journal of Geophysical Research: Solid Earth*, *110*(B3).
Duan, B. and Oglesby, D.D., 2006. Heterogeneous fault stresses from previous earthquakes and the effect on dynamics of parallel strike-slip faults. *Journal of Geophysical Research: Solid Earth*, *111*(B5).
Duan, B. and Oglesby, D.D., 2007. Nonuniform prestress from prior earthquakes and the effect on dynamics of branched fault systems. *Journal of Geophysical Research: Solid Earth*, *112*(B5).
Fattaruso, L.A., Cooke, M.L. and Dorsey, R.J., 2014. Sensitivity of uplift patterns to dip of the San Andreas fault in the Coachella Valley, California. *Geosphere*, *10*(6), pp.1235-1246.
Fay, N.P. and Humphreys, E.D., 2005. Fault slip rates, effects of elastic heterogeneity on geodetic data, and the strength of the lower crust in the Salton Trough region, southern California. *Journal of Geophysical Research: Solid Earth*, *110*(B9).
Field, E.H., Arrowsmith, R.J., Biasi, G.P., Bird, P., Dawson, T.E., Felzer, K.R., Jackson, D.D., Johnson, K.M., Jordan, T.H., Madden, C. and Michael, A.J., 2014. Uniform California earthquake rupture forecast, version 3 (UCERF3)—The time-independent model. *Bulletin of the Seismological Society of America*, *104*(3), pp.1122-1180.
Fosdick, J.C. and Bisniuk, K., 2018. Sedimentary signals of recent faulting along an old strand of the San Andreas Fault, USA. *Scientific reports,* 8(1), p.12132.
Fulton, P.M., Brodsky, E.E., Kano, Y., Mori, J., Chester, F., Ishikawa, T., Harris, R.N., Lin, W., Eguchi, N. and Toczko, S., 2013. Low coseismic friction on the Tohoku-Oki fault determined from temperature measurements. *Science*, *342*(6163), pp.1214-1217.
Fumal, T.E., Rymer, M.J. and Seitz, G.G., 2002. Timing of large earthquakes since AD 800 on the Mission Creek strand of the San Andreas fault zone at Thousand Palms Oasis, near Palm Springs, California. *Bulletin of the Seismological Society of America*, *92*(7), pp.2841-2860.
Goebel, T.H.W., Hauksson, E., Shearer, P.M. and Ampuero, J.P., 2015. Stress-drop

heterogeneity within tectonically complex regions: a case study of San Gorgonio Pass, southern California. *Geophysical Journal International*, *202*(1), pp.514-528.

Goldsby, D.L. and Tullis, T.E., 2011. Flash heating leads to low frictional strength of crustal rocks at earthquake slip rates. *Science*, *334*(6053), pp.216-218.

Hardebeck, J.L. and Hauksson, E., 2001. Crustal stress field in southern California and its implications for fault mechanics. *Journal of Geophysical Research: Solid Earth*, *106*(B10), pp.21859-21882.

Hart, E.W., Bryant, W.A., and J.A. Treiman, 1993. Surface faulting associated with the June 1992 Landers earthquake, California. *Calif. Geol.* 46, pp.10-16.

Heermance, R.V. and Yule, D., 2017. Holocene slip rates along the San Andreas Fault System in the San Gorgonio Pass and implications for large earthquakes in southern California. *Geophysical Research Letters*, *44*(11), pp.5391-5400.

Herbert, J.W. and Cooke, M.L., 2012. Sensitivity of the southern San Andreas fault system to tectonic boundary conditions and fault configurations. *Bulletin of the Seismological Society of America*, *102*(5), pp.2046-2062.

Herbert, J.W., Cooke, M.L. and Marshall, S.T., 2014a. Influence of fault connectivity on slip rates in southern California: Potential impact on discrepancies between geodetic derived and geologic slip rates. *Journal of Geophysical Research: Solid Earth*, *119*(3), pp.2342-2361.

Kame, N., Rice, J.R. and Dmowska, R., 2003. Effects of prestress state and rupture velocity on dynamic fault branching. *Journal of Geophysical Research: Solid Earth*, *108*(B5).

Kase, Y. and Day, S.M., 2006. Spontaneous rupture processes on a bending fault. *Geophysical Research Letters*, *33*(10).

Kendrick, K.J. and Fumal, T.E., 2005, October. Paleoseismicity of the northern San Jacinto fault, Colton and San Bernardino, southern California; preliminary results. In *2005 Salt Lake City Annual Meeting*.

Kendrick, K.J., Matti, J.C. and Mahan, S.A., 2015. Late Quaternary slip history of the Mill Creek strand of the San Andreas fault in San Gorgonio Pass, southern California: The role of a subsidiary left-lateral fault in strand switching. *Bulletin*, *127*(5-6), pp.825-849.

King, G.C., Stein, R.S. and Lin, J., 1994. Static stress changes and the triggering of earthquakes. *Bulletin of the Seismological Society of America*, *84*(3), pp.935-953.

Li, H., Xue, L., Brodsky, E.E., Mori, J.J., Fulton, P.M., Wang, H., Kano, Y., Yun, K., Harris, R.N., Gong, Z. and Li, C., 2015. Long-term temperature records following the Mw 7.9 Wenchuan (China) earthquake are consistent with low friction. *Geology*, *43*(2), pp.163-166.

Loveless, J.P. and Meade, B.J., 2011. Stress modulation on the San Andreas fault by interseismic fault system interactions. *Geology*, *39*(11), pp.1035-1038.

Lozos, J.C., Oglesby, D.D., Brune, J.N. and Olsen, K.B., 2012. Small intermediate fault segments can either aid or hinder rupture propagation at stepovers. *Geophysical Research Letters*, *39*(18).

Lozos, J.C., 2016. A case for historic joint rupture of the San Andreas and San Jacinto faults. *Science advances*, *2*(3), p.e1500621.

Madden, E.H. and Pollard, D.D., 2012. Integration of surface slip and aftershocks to constrain the 3D structure of faults involved in the M 7.3 Landers earthquake, Southern California. *Bulletin of the Seismological Society of America*, *102*(1), pp.321-342.

Maerten, L., Willemse, E.J., Pollard, D.D. and Rawnsley, K., 1999. Slip distributions on intersecting normal faults. *Journal of Structural Geology*, *21*(3), pp.259-272.

Marshall, S.T., Cooke, M.L. and Owen, S.E., 2009. Interseismic deformation associated with three-dimensional faults in the greater Los Angeles region, California. *Journal of Geophysical Research: Solid Earth*, *114*(B12).

Matti, J.C., Morton, D.M. and Cox, B.F., 1992. *The San Andreas fault system in the vicinity of the central Transverse Ranges province, southern California* (No. 92-354). US Geological Survey,.

McGill, S., Dergham, S., Barton, K., Berney-Ficklin, T., Grant, D., Hartling, C., Hobart, K., Minnich, R., Rodriguez, M., Runnerstrom, E. and Russell, J., 2002. Paleoseismology of the San Andreas fault at Plunge Creek, near San Bernardino, southern California. *Bulletin of the Seismological Society of America*, *92*(7), pp.2803-2840.

McPhillips, D. and Scharer, K.M., 2018. Quantifying uncertainty in cumulative surface slip along the Cucamonga Fault, a crustal thrust fault in southern California. *Journal of Geophysical Research: Solid Earth*, *123*(10), pp.9063-9083.

Meade, B.J. and Hager, B.H., 2005. Block models of crustal motion in southern California constrained by GPS measurements. *Journal of Geophysical Research: Solid Earth*, *110*(B3).

Nicholson, C., Plesch, A., and Shaw, J.H., 2017. Community Fault Model Version 5.2: Updating and expanding the CFM 3D fault set and its associated fault database: Poster Presentation at 2017 Southern California Earthquake Center (SCEC) Annual Meeting.

Oglesby, D.D., Day, S.M. and O'Connell, D.R., 2003. Dynamic and static interaction of two thrust faults: A case study with general implications. *Journal of Geophysical Research: Solid Earth*, *108*(B10).

Oglesby, D.D., 2005. The dynamics of strike-slip step-overs with linking dip-slip faults. *Bulletin of the Seismological Society of America*, *95*(5), pp.1604-1622.

Onderdonk, N.W., Rockwell, T.K., McGill, S.F. and Marliyani, G.I., 2013. Evidence for seven surface ruptures in the past 1600 years on the Claremont fault at Mystic Lake, northern San Jacinto fault zone, California. *Bulletin of the Seismological Society of America*, *103*(1), pp.519-541.

Onderdonk, N.W., McGill, S.F. and Rockwell, T.K., 2015. Short-term variations in slip rate and size of prehistoric earthquakes during the past 2000 years on the northern San Jacinto fault zone, a major plate-boundary structure in southern California. *Lithosphere*, *7*(3), pp.211-234.

Onderdonk, N., McGill, S. and Rockwell, T., 2018. A 3700 yr paleoseismic record from the northern San Jacinto fault and implications for joint rupture of the San Jacinto and San Andreas faults. *Geosphere*, *14*(6), pp.2447-2468.

Philibosian, B., Fumal, T. and Weldon, R., 2011. San Andreas fault earthquake chronology and Lake Cahuilla history at Coachella, California. *Bulletin of the Seismological Society of America*, *101*(1), pp.13-38.

Plesch, A., Shaw, J.H., Benson, C., Bryant, W.A., Carena, S., Cooke, M., Dolan, J., Fuis, G., Gath, E., Grant, L. and Hauksson, E., 2007. Community fault model (CFM) for southern California. *Bulletin of the Seismological Society of America*, *97*(6), pp.1793-1802.

Pollitz, F.F. and Sacks, I.S., 2002. Stress triggering of the 1999 Hector Mine earthquake by transient deformation following the 1992 Landers earthquake. *Bulletin of the Seismological Society of America*, *92*(4), pp.1487-1496.

Richards-Dinger, K. and Dieterich, J.H., 2012. RSQSim earthquake simulator. *Seismological Research Letters*, *83*(6), pp.983-990.

Rockwell, T.K., Dawson, T.E., Ben-Horin, J.Y. and Seitz, G., 2015. A 21-event, 4,000-year history of surface ruptures in the Anza seismic gap, San Jacinto Fault, and implications for long-term earthquake production on a major plate boundary fault. *Pure and Applied*

Geophysics, *172*(5), pp.1143-1165.

Rockwell, T.K., Meltzner, A.J. and Haaker, E.C., 2018. Dates of the Two Most Recent Surface Ruptures on the Southernmost San Andreas Fault Recalculated by Precise Dating of Lake Cahuilla Dry Periods. *Bulletin of the Seismological Society of America*, *108*(5A), pp.2634-2649.

Seitz, G., Weldon II, R. and Biasi, G.P., 1997. The Pitman Canyon paleoseismic record: A re-evaluation of southern San Andreas fault segmentation. *Journal of Geodynamics*, *24*(1-4), pp.129-138.

Sharp, R.V., 1981. Variable rates of late Quaternary strike slip on the San Jacinto fault zone, southern California. *Journal of Geophysical Research: Solid Earth*, *86*(B3), pp.1754-1762.

Sieh, K.E., 1986. Slip rate across the San Andreas fault and prehistoric earthquakes at Indio, California. *Eos Trans. AGU*, *67*(44), p.1200.

Sieh, K.E. and Williams, P.L., 1990. Behavior of the southernmost San Andreas fault during the past 300 years. *Journal of Geophysical Research: Solid Earth*, *95*(B5), pp.6629-6645.

Sieh, K., Jones, L., Hauksson, E., Hudnut, K., Eberhart-Phillips, D., Heaton, T., Hough, S., Hutton, K., Kanamori, H., Lilje, A. and Lindvall, S., 1993. Near-field investigations of the Landers earthquake sequence, April to July 1992. *Science*, *260*(5105), pp.171-176.

Simpson, R.W., 1997. Quantifying Anderson's fault types. *Journal of Geophysical Research: Solid Earth*, *102*(B8), pp.17909-17919.

Smith, B.R. and Sandwell, D.T., 2006. A model of the earthquake cycle along the San Andreas Fault System for the past 1000 years. *Journal of Geophysical Research: Solid Earth*, *111*(B1).

Smith-Konter, B. and Sandwell, D., 2009. Stress evolution of the San Andreas fault system: Recurrence interval versus locking depth. *Geophysical Research Letters*, *36*(13).

Stein, R.S., 1999. The role of stress transfer in earthquake occurrence. *Nature*, *402*(6762), p.605.

Tarnowski, J.M., 2017. *The Effects of Dynamic Stress on Fault Interaction and Earthquake Triggering in the San Gorgonio Pass and San Jacinto, CA Regions*. University of California, Riverside.

Thomas, A.L., 1993. *Poly 3 D: a three-dimensional, polygonal element, displacement discontinuity boundary element computer program with applications to fractures, faults, and cavities in the Earth's crust* (Master's thesis, to the Department of Geology.Stanford University).

Tong, X., Smith-Konter, B. and Sandwell, D.T., 2014. Is there a discrepancy between geological and geodetic slip rates along the San Andreas Fault System?. *Journal of Geophysical Research: Solid Earth*, *119*(3), pp.2518-2538.

Weldon, R.J. and Sieh, K.E., 1985. Holocene rate of slip and tentative recurrence interval for large earthquakes on the San Andreas fault, Cajon Pass, southern California. *Geological Society of America Bulletin*, *96*(6), pp.793-812.

Weldon, R.J., Fumal, T.E., Powers, T.J., Pezzopane, S.K., Scharer, K.M. and Hamilton, J.C., 2002. Structure and earthquake offsets on the San Andreas fault at the Wrightwood, California, paleoseismic site. *Bulletin of the Seismological Society of America*, *92*(7), pp.2704-2725.

Willemse, E.J. and Pollard, D.D., 1998. On the orientation and patterns of wing cracks and solution surfaces at the tips of a sliding flaw or fault. *Journal of Geophysical Research: Solid Earth*, *103*(B2), pp.2427-2438.

Yule, D. and Howland, C., 2001. A revised chronology of earthquakes produced by the San Andreas fault at Burro Flats, near Banning, California. In *SCEC Annual Meeting, Proceedings* *and Abstracts*.

Yule, D. and Sieh, K., 2003. Complexities of the San Andreas fault near San Gorgonio Pass: Implications for large earthquakes. *Journal of Geophysical Research: Solid Earth*, *108*(B11).

Yule, D., Scharer, K., Sieh, K., Wolff, L., McBurnett, P., Ramzan, S., Witkosky, R. and Desjarlais, I., 2014. Paleoseismology and slip rate of the San Andreas fault system at San Gorgonio Pass.

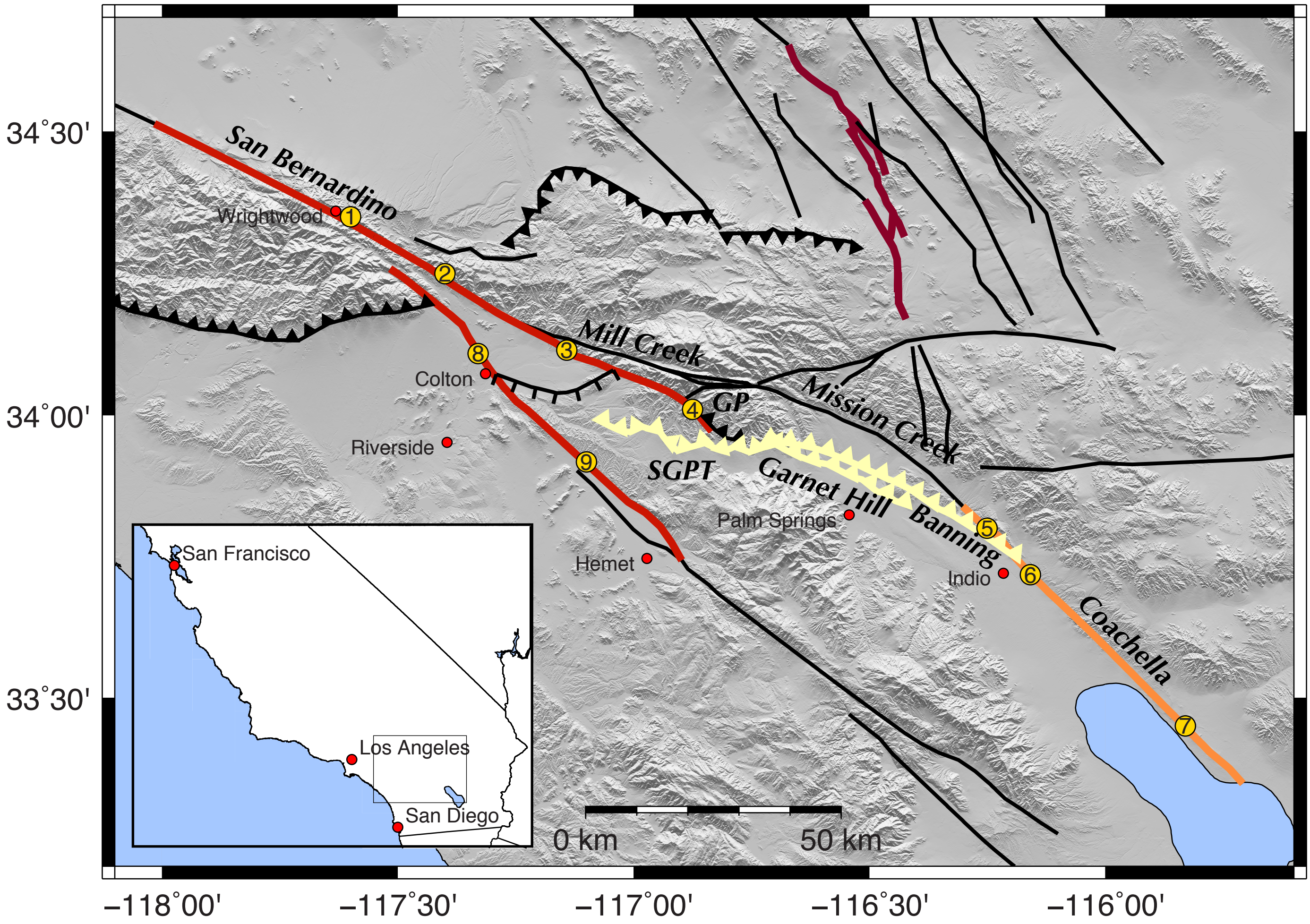
San Bernardino
Wrightwood
Mill Creek
Colton
Riverside
GP
Mission Creek
SGPT
Garnet Hill
Banning
Palm Springs
Hemet
Indio
Coachella
San Francisco
Los Angeles
San Diego
0 km
50 km
34˚30'
34˚00'
33˚30'
−118˚00'
−117˚30'
−117˚00'
−116˚30'
−116˚00'
1
2
3
4
5
6
7
8
9

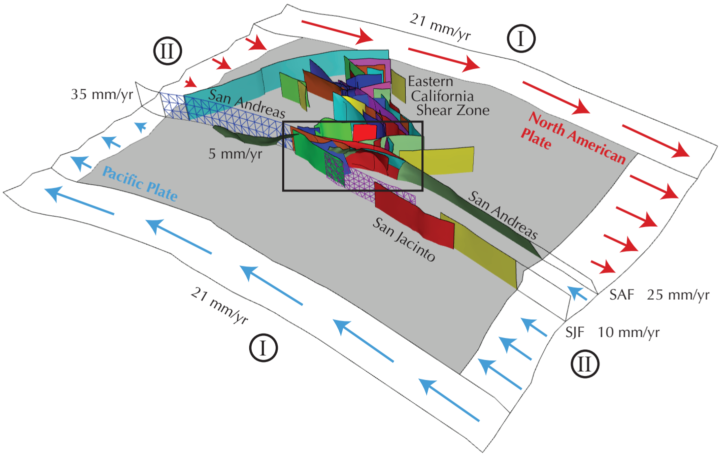

21 mm/yr
I
II
35 mm/yr
San Andreas
Eastern
California
Shear Zone
North American
Plate
5 mm/yr
Pacific Plate
San Andreas
San Jacinto
SAF 25 mm/yr
SJF 10 mm/yr
21 mm/yr
I
II

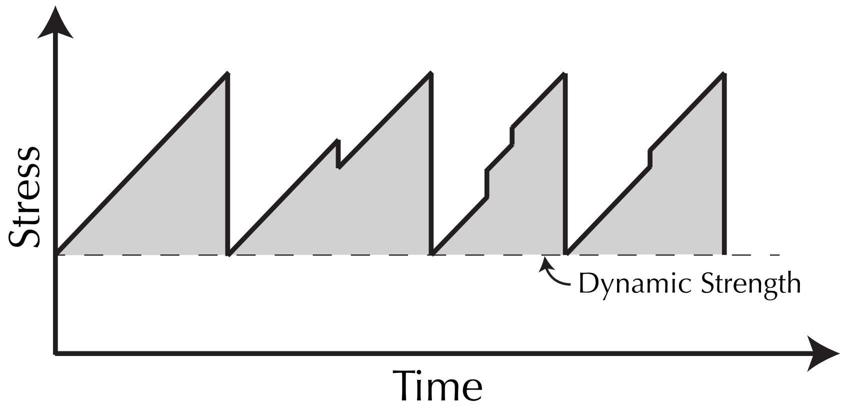
Stress
Dynamic Strength
Time

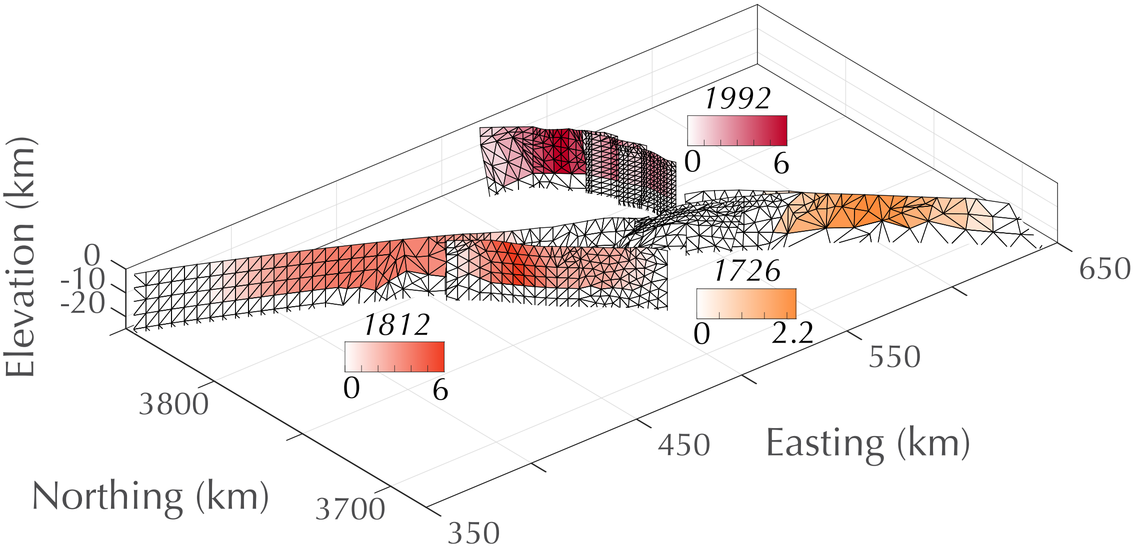
1992
0
6
1726
0
2.2
1812
0
6
Elevation (km)
0
-10
-20
3800
3700
Northing (km)
350
450
550
650
Easting (km)

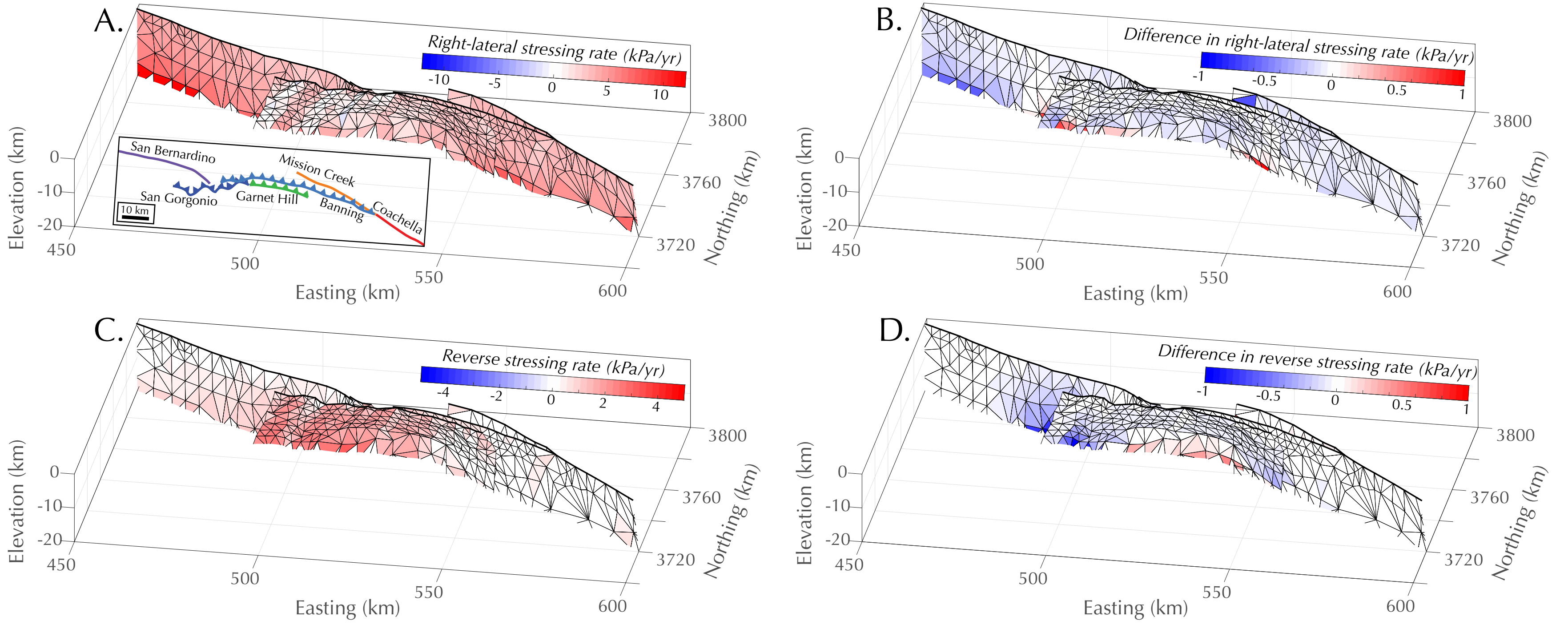

A.
Right-lateral stressing rate (kPa/yr)
-10
-5
0
5
10
San Bernardino
Mission Creek
San Gorgonio
Garnet Hill
Banning
Coachella
10 km
Elevation (km)
0
-10
-20
450
500
550
600
Easting (km)
3800
3760
3720
Northing (km)
B.
Difference in right-lateral stressing rate (kPa/yr)
-1
-0.5
0
0.5
1
C.
Reverse stressing rate (kPa/yr)
-4
-2
0
2
4
D.
Difference in reverse stressing rate (kPa/yr)
-1
-0.5
0
0.5
1

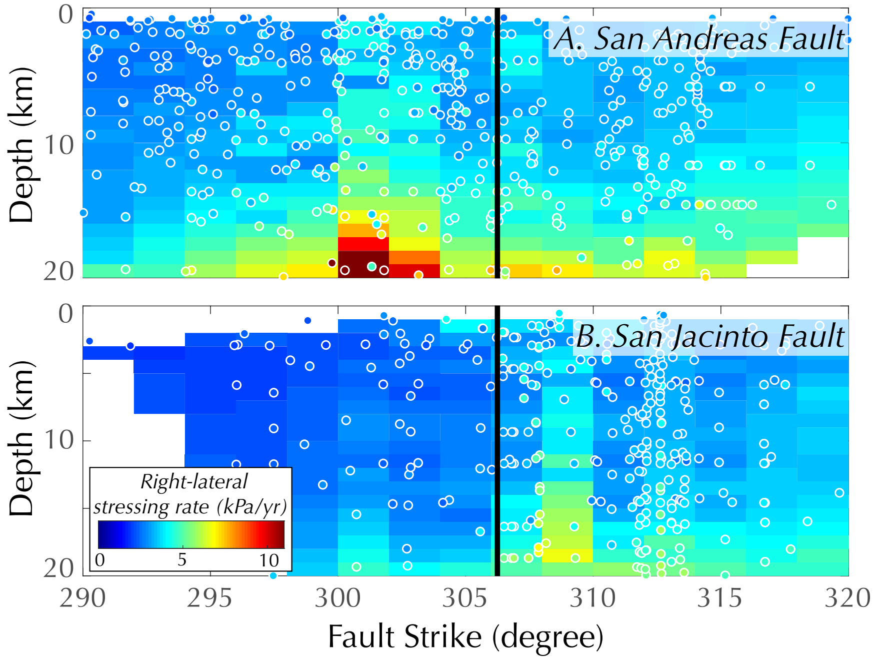

A. San Andreas Fault
B. San Jacinto Fault
Depth (km)
Depth (km)
Right-lateral stressing rate (kPa/yr)
0
5
10
0
10
20
290
295
300
305
310
315
320
Fault Strike (degree)

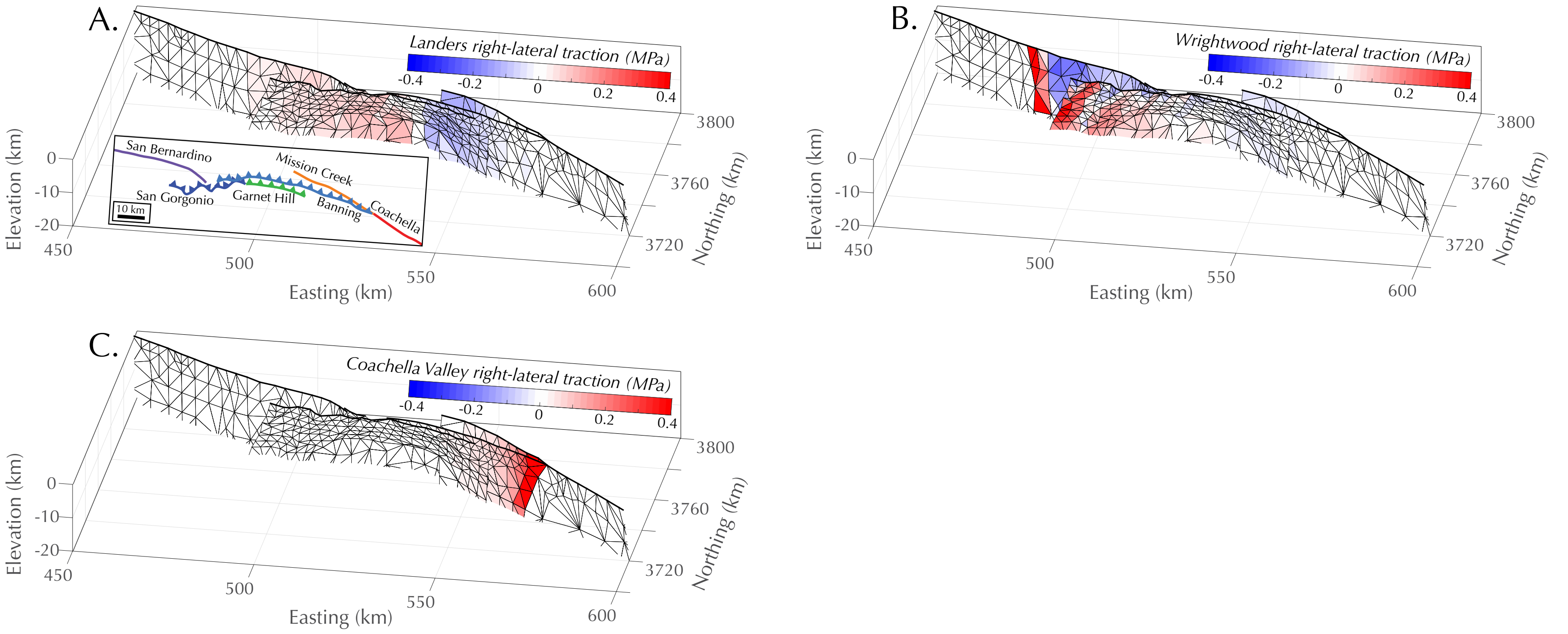
A.
Landers right-lateral traction (MPa)
-0.4 -0.2 0 0.2 0.4
San Bernardino
Mission Creek
San Gorgonio
Garnet Hill
Banning
Coachella
10 km
Elevation (km)
0 -10 -20
450 500 550 600
Easting (km)
3800 3760 3720
Northing (km)
B.
Wrightwood right-lateral traction (MPa)
-0.4 -0.2 0 0.2 0.4
Elevation (km)
0 -10 -20
450 500 550 600
Easting (km)
3800 3760 3720
Northing (km)
C.
Coachella Valley right-lateral traction (MPa)
-0.4 -0.2 0 0.2 0.4
Elevation (km)
0 -10 -20
450 500 550 600
Easting (km)
3800 3760 3720
Northing (km)

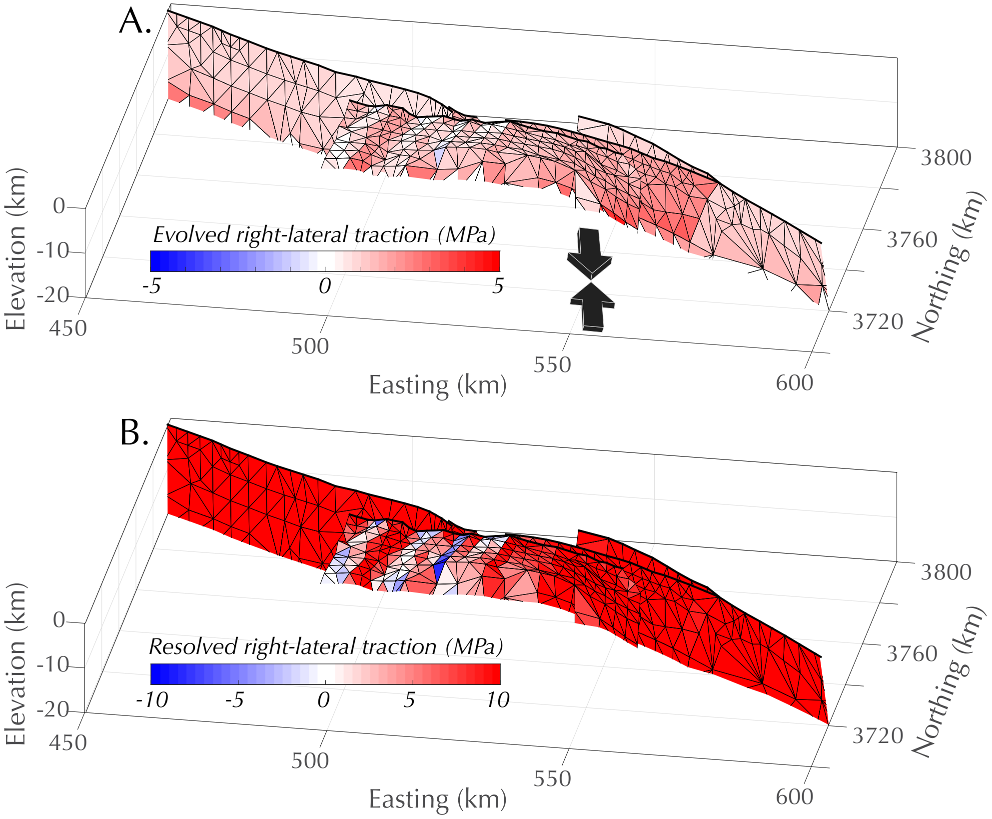
A.
Evolved right-lateral traction (MPa)
-5
0
5
Elevation (km)
0
-10
-20
450
500
550
600
Easting (km)
3800
3760
3720
Northing (km)
B.
Resolved right-lateral traction (MPa)
-10
-5
0
5
10
Elevation (km)
0
-10
-20
450
500
550
600
Easting (km)
3800
3760
3720
Northing (km)

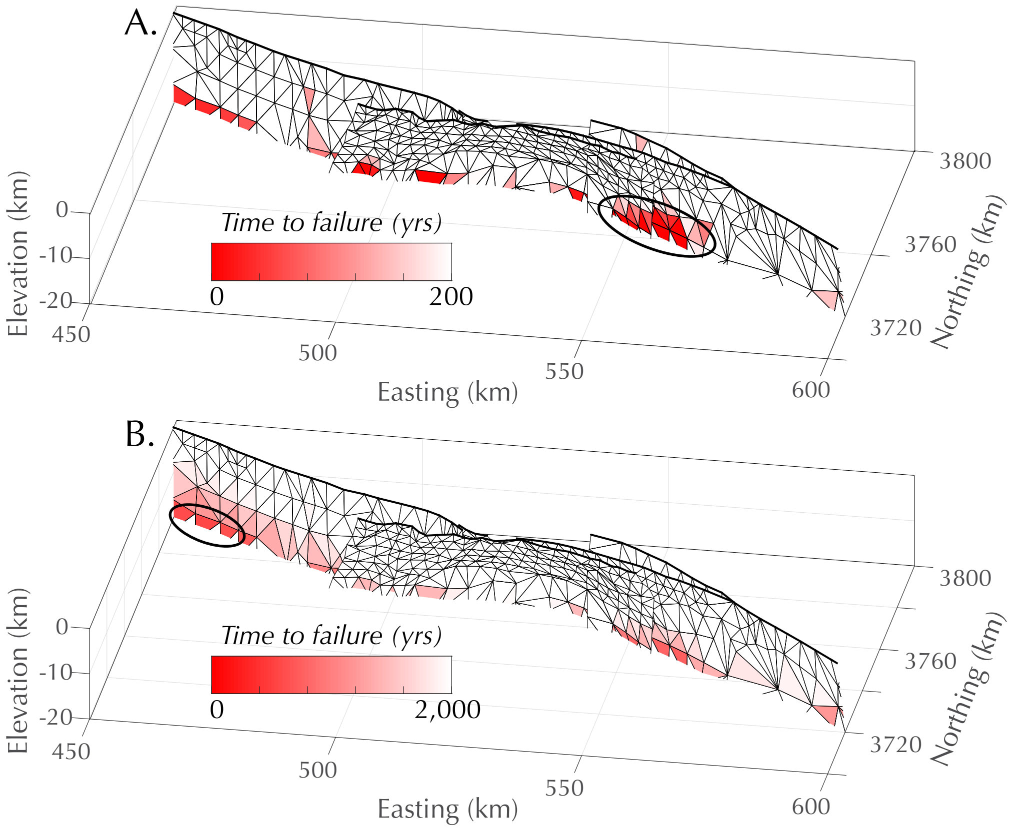
A.
Time to failure (yrs)
0
200
Elevation (km)
0
-10
-20
450
500
550
600
Easting (km)
3800
3760
3720
Northing (km)
B.
Time to failure (yrs)
0
2,000
Elevation (km)
0
-10
-20
450
500
550
600
Easting (km)
3800
3760
3720
Northing (km)

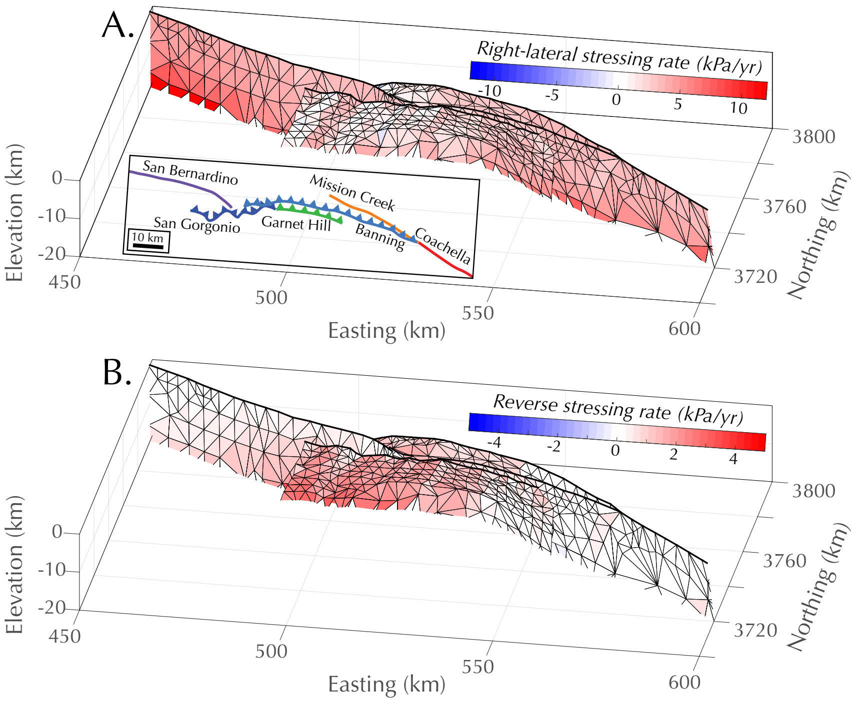

Figure S1. Right-lateral (A) and reverse dip slip (B) stressing rates for the alternative fault configuration from Beyer et al. (2018).